Intraplate volcanism originating from upwelling hydrous mantle transition zone

Jianfeng Yang, Manuele Faccenda*

Dipartimento di Geoscienze, Università di Padova, 35131 Padova, Italy

Most magmatism occurring on Earth is conventionally attributed to passive mantle upwelling at mid-ocean ridges, slab devolatilization at subduction zones, and mantle plumes. However, the widespread Cenozoic intraplate volcanism in northeast China[1-3] and the peculiar petit-spot volcanoes[4-7] offshore the Japan trench cannot be readily associated with any of these mechanisms. In addition, the mantle beneath this type of volcanism is characterized by seismic low velocity zones (LVZs) present above and below the transition zone[8-12], and a comprehensive interpretation of all these intriguing phenomena is lacking. Here we show that most if not all the intraplate and petit-spot volcanism and LVZs present around the Japanese subduction zone can be explained by the Cenozoic interaction of the subducting Pacific slab with a hydrous transition zone. Numerical modelling results indicate that 0.2-0.3 wt.% H_2O dissolved in mantle minerals which are driven out from the transition zone in response to subduction and retreat of a stagnant plate is sufficient to reproduce the observations. This suggests that a critical amount of water may have accumulated in the transition zone around this subduction zone as well as others of the Tethyan tectonic belt[13] characterized by intraplate/petit-spot volcanism and LVZs in the underlying mantle.

The Cenozoic intraplate volcanism in northeast China is located more than 1000 km westward of the Japan trench[1], while the young alkaline basalts (0-6 Ma) known as petit-spots outcrop up to 600 km eastward of the trench[4] (Fig. 1). The formation mechanism of these types of on- and off-shore volcanism is still debated as there is no geological and geophysical correlation with mantle plumes or arc volcanism[6,14].

Seismic tomography models indicate that in this region the Pacific Plate is currently stagnant in the transition zone, extending continuously up to nearly 1000 km to the inland of northeast China[3,8,10]. Thus, it has been proposed that the Cenozoic intraplate magmatism is related to the dehydration of the Pacific slab in the mantle transition zone (MTZ) between ~410 km and ~660 km depth[2,15].

The primary petit-spot magma has been determined volatile-rich with extremely EM 1-like isotopic compositions[6,7]. The lack of hotspot tracks in this region excludes the contribution from a mantle plume. It has been postulated that the petit-spot magma forms in the asthenosphere, and migrates upward through the oceanic lithosphere by reactive porous flow in response to plate flexure[4,6,7].

Based on electrical conductivity surveys, the transition zone probably holds circa 0.1 wt.% water[16], while the transition zone below China and Japan are particularly wet with at least 0.5-1 wt.% water[17]. The MTZ is primarily composed of wadsleyite and ringwoodite minerals that can accommodate 1-3 wt.% water, which is 1 to 2 orders of magnitude higher than the water (hydrogen) solubility in upper and lower mantle minerals. Given the large contrast in water solubility between the MTZ and upper/lower mantle, it is reasonable to expect deep dehydration melting when subducting slabs excite vertically flow in the nearby wet MTZ[18]. Indeed, seismic low velocity zones (LVZs) above 410 km and below 660 km have been observed not only in Japan[8-12,14,15], but also around subduction zones in Europe[19] and western US[20,21].

To test this hypothesis, we construct two-dimensional numerical experiments in which a self-sustained oceanic plate subduction is characterized by trench retreat and slab stagnation into a homogeneously or heterogeneously wet MTZ (Methods). The subducting plate and entrained dry upper mantle push the adjacent wet MTZ downward to the lower mantle such that a partially molten layer forms between 700 and 800 km depth (Fig. 2a, M2) (Supplementary Video 1). On the other hand, MTZ material uplifted to the upper mantle starts to partially melt above 410-km (Fig. 2a, M3). Slab stagnation and retreat is accompanied by subslab MTZ upwelling and new melting (M1). These partially molten regions above and below the MTZ cause significant seismic LVZs (Fig. 2c). When melt percolation is active (Methods), extraction to the surface occurs forming intraplate and petit-spot volcanisms ahead of and behind the trench, respectively.

Figure 3 shows the spatial and temporal trend of modelled volcanics for the reference model in Fig. 2. The first intraplate volcanism occurs ~500 km away from the trench, then it spreads to two opposite directions. The mantle water content decreases after melt extraction, which precludes further deep (≥200 km) melting of the residual peridotite (Fig. 2b). As the slab rolls back, more distal wet MTZ is sucked into the upper mantle wedge, such that partial melting and volcanoes will form further away from the trench. The new generated volcanism is not homogeneously distributed as it is strongly influenced by mantle flow and trench movement. Furthermore, a heterogeneous distribution of water in the MTZ would prevent the formation of any temporal-spatial magmatic sequence as wetter portions would melt earlier than drier regions at the same P-T conditions. It is noteworthy that intraplate volcanism also occurs few hundred kilometers in front of the slab tip. At ~12 Myr, petit-spot volcanoes behind the trench appear, they are located at the trench up to ~300 km far away and exhibit a similar magmatic activity trend as the intraplate volcanism.

We further test the influence of initial water content in the transition zone and other parameters on the genesis of asthenospheric melting (Extended Data Fig. 5). Melting commences 40 km above the transition zone and no petit-spot volcanoes are formed for 0.2 wt.% initial water. The thickness of the partially molten layer could be few tens of km to more than 100 km, depending on the melt extraction efficiency and water content. Petit-spot volcano might locate more than 600 km away from the trench if melt extraction process is readily efficient (Extended Data Fig. 5b). Given the assumed homogeneous distribution of water in the MTZ, these models provide upper bound estimates on the volumes of volcanics and melt. However, the results hold also in case of a more realistic heterogeneous distribution of the water in this mantle level (Extended Data Fig. 5e).

When comparing the model results with seismic and geological observations, we note that around the Pacific slab three remarkable seismic low velocity zones outward of the transition zone are clearly imaged which are well correlated with the locations of intraplate and petit-spot volcanoes, and the modelled partially molten zones (Figs. 1-2). Although seismic low velocity anomalies are generally attributed to thermal effects[14], presence of water[22], melt[11,20] and/or major element compositional heterogeneities[16,23], it has been recently argued that some of these LVZs could be seismic anisotropy-induced artifacts[24]. Nevertheless, the authenticity of the subslab LVZ1 and LVZ2 appearing in tomographic models have been confirmed by other independent studies using, respectively, an accurate scrutiny of the seismic ray paths[25] sampling the LVZ1 and receiver functions[11]. The LVZ3 sits below the active Changbai volcano and appears to extend down to 410 km as clearly revealed by multiple high-resolution tomography models[3,8,15,26]. A thermal anomaly from a non-hotspot upwelling, if hypothetically exists, is hardly reconcilable with the large velocity drop of LVZ1. The hot material will rapidly cool down when flowing upward by adiabatic decompression and the latent heat of the wadsleyite to olivine reaction. Laboratory experiments show that seismic wave speeds are insensitive to moderate (< 1wt. %) water contents for olivine[27] and wadsleyite[22], thus the LVZs are very likely to be caused by partial melting and/or compositional heterogeneities. The presence of basalts at the bottom of the upper mantle should be excluded as it would generate a positive seismic anomaly[28]. On the other hand, basalts accumulating at the base of the MTZ could be effectively dragged by the slab into the uppermost lower mantle and generate the LVZ2. However, receiver functions indicate that the lower mantle LVZs are within the 750-780 km depth range[11], which is likely below the post-garnet phase transition where basalts are seismically faster than mantle rocks.

The presence of melt in the deep mantle, which is mostly catalyzed by volatiles involvement, decreases seismic velocities and provides a magmatic source for intraplate/petit-spot volcanism. Our numerical models thereby suggest that a hydrous transition zone with at least 0.2-0.3 wt.% water beneath northeast China and offshore Japan can comprehensively explain the LVZs, and the intraplate and petit-spot volcanism. This model does not exclude the devolatilization of the stagnant Pacific slab as a mechanism to explain the LVZ3 region and the overlying intraplate volcanism[15], which favors the upwelling of volatile-rich plumes from the MTZ[29] as envisaged by the Big Mantle Wedge model[15,30]. However, the same slab-derived volatiles cannot obviously be the cause of the LVZ1 and LVZ2 and of the petit-spots, implying the presence of a metasomatized MTZ before the last subduction episode. The accumulation of water in the MTZ could be caused by, for example, delamination of volatile-rich lithospheric roots[31] or by previous slab dehydration episodes in the MTZ and subsequent absorption of the water by wadsleyite and ringwoodite. Alongside with water, reduced (by redox-freezing) carbonated sources and restitic, K-hollandite-bearing sediments are required to explain the volatile-rich, alkaline and EM1-type petrological and geochemical signature of the basalts[32,33]. This is not surprising since the MTZ, a graveyard for stagnating slabs, is the most likely candidate to host volatiles and subducted sediments, and long-term isolation of these MTZ domains would be consistent with the ancient metasomatizing episodes estimated for intraplate basalts[32-34]. Subsequent subduction events would mobilize the wet and (carbon + alkali)-bearing MTZ rocks promoting the formation of silica undersaturated magmas in the upper mantle. It is important to note that the addition of these components is not critical to our results because the location and amounts of partial melting atop and below the MTZ will still be dictated by the distribution of wet MTZ domains, while reduced carbonated sources are expected to experience redox melting at shallower depths (<250 km)[35]. The process proposed here could potentially explain also the Cenozoic anorogenic volcanism in the Mediterranean[13] and intraplate volcanism in the Turkish-Iranian Plateau[36] regions characterized by the long-term subduction of Tethys ocean. Together with surface intraplate/petit-spot volcanism, constraints on deep seismic low velocities and/or high electrical conductivity may thus indicate a volatile-rich and/or partially molten mantle within and around the transition zone.

Data availability The dataset generated during the current study are available at https://figshare.com/articles/Yang_Faccenda_Nature2019/9933056.

Code availability Requests about the numerical modelling codes associated with this paper should be sent to the main code developer (taras.gerya@erdw.ethz.ch). The numerical 2D finite element code MVEP2 (https://bitbucket.org/bkaus/mvep2) was used for the two-phase flow model in Extended Data Figure 6.

References

1. Chen, Y., Zhang, Y., Graham, D., Su, S. & Deng, J. Geochemistry of Cenozoic basalts and mantle xenoliths in Northeast China. Lithos **96**, 108-126 (2007).
2. Wang, X.-C., Wilde, S. A., Li, Q.-L. & Yang, Y.-N. Continental flood basalts derived from the hydrous mantle transition zone. Nat. Commun. **6**, 7700 (2015).
3. Chen, C. et al. Mantle transition zone, stagnant slab and intraplate volcanism in Northeast Asia. Geophys. J. Int. **209**, 68-85 (2017).
4. Hirano, N. et al. Volcanism in response to plate flexure. Science **313**, 1426-1428 (2006).
5. Okumura, S. & Hirano, N. Carbon dioxide emission to Earth's surface by deep-sea volcanism. Geology **41**, 1167-1170 (2013).
6. Machida, S. *et al.* Petit-spot geology reveals melts in upper-most asthenosphere dragged by lithosphere. Earth Planet. Sci. Lett. **426**, 267-279 (2015).
7. Pilet, S. et al. Pre-subduction metasomatic enrichment of the oceanic lithosphere induced by plat flexure. Nat. Geosci. **9**, 898 (2016).
8. Li, C., Van der Hilst, R. D., Meltzer, A. S. & Engdahl, E. R. Subduction of the Indian lithosphere beneath the Tibetan Plateau and Burma. Earth Planet. Sci. Lett. **274**, 157-168 (2008).
9. Tauzin, B., Debayle, E. & Wittlinger, G. Seismic evidence for a global low-velocity layer within the Earth's upper mantle. Nat. Geosci. **3**, 718 (2010).
10. Fukao, Y. & Obayashi, M. Subducted slabs stagnant above, penetrating through, and trapped below the 660 km discontinuity. J. Geophys. Res.: Solid Earth **118**, 5920-5938 (2013).
11. Liu, Z., Park, J. & Karato, S.-i. Seismological detection of low velocity anomalies surrounding the mantle transition zone in Japan subduction zone. Geophys. Res. Lett. **43**, 2480-2487 (2016).
12. Wei, S. S. & Shearer, P. M. A sporadic low-velocity layer atop the 410 km discontinuity beneath the Pacific Ocean. J. Geophys. Res.: Solid Earth **122**, 5144-5159 (2017).
13. Lustrino, M. & Wilson, M. The circum-Mediterranean anorogenic Cenozoic igneous province. Earth Sci. Rev. **81**, 1-65 (2007).
14. Tang, Y. et al. Changbaishan volcanism in northeast China linked to subduction-induced mantle upwelling. Nat. Geosci. **7**, 470 (2014).
15. Zhao, D., tian, Y., Lei, J., Liu, L., Zheng, S. Seismic image and origin of the Changbai intraplate volcano in East Asia: Role of big mantle wedge above the stagnant Pacific slab. Phys. Earth Planet. Lett. **173**, 197-206 (2009).
16. Karato, S.-i. Water distribution across the mantle transition zone and its implications for global material circulation. Earth Planet. Sci. Lett. **301**, 413-423 (2011).
17. Kelbert, A., Schultz, A. & Egbert, G. Global electromagnetic induction constraints on transition-zone water content variations. Nature **460**, 1003 (2009).
18. Bercovici, D. & Karato, S.-i. Whole-mantle convection and the transition-zone water filter. Nature **425**, 39-44 (2003).
19. Liu, Z., Park, J. & Karato, S.-i. Seismic evidence for water transport out of the mantle transition zone beneath the European Alps. Earth Planet. Sci. Lett. **482**, 93-104 (2018).
20. Schmandt, B., Jacobsen, S. D., Becker, T. W., Liu, Z. & Dueker, K. G. Dehydration melting at the top of the lower mantle. Science **344**, 1265-1268 (2014).
21. Hier-Majumder, S. & Tauzin, B. Pervasive upper mantle melting beneath the western US. Earth Planet. Sci. Lett. **463**, 25-35 (2017).
22. Mao, Z. et al. Elasticity of hydrous wadsleyite to 12 GPa: implications for Earth's transition zone. Geophys. Res. Lett. **35** (2008).
23. Irifune, T. et al. Sound velocities of majorite garnet and the composition of the mantle transition region. Nature **451**, 814 (2008).

24. Bezada, M., Faccenda, M. & Toomey, D. Representing anisotropic subduction zones with isotropic velocity models: A characterization of the problem and some steps on a possible path forward. Geochem. Geophys. Geosy. **17**, 3164-3189 (2016).
25. Obayashi, M., Sugioka, H., Yoshimitsu, J. & Fukao, Y. High temperature anomalies oceanward of subducting slabs at the 410-km discontinuity. Earth Planet. Sci. Lett. **243**, 149-158 (2006).
26. Zhao, D. & Tian, Y. Changbai intraplate volcanism and deep earthquakes in East Asia: a possible link? Geophys. J. Int. **195**, 706-724 (2013).
27. Cline II, C. J., Faul, U. H., David, E. C., Berry, A. J. & Jackson, I. Redox-influenced seismic properties of upper-mantle olivine. Nature **555**, 355 (2018).
28. Xu, W., Lithgow-Bertelloni, C., Stixrude, L. & Ritsema, J. The effect of bulk composition and temperature on mantle seismic structure. Earth Planet. Sci. Lett. **275**, 70-79 (2008).
29. Litasov, K. D., Shatskiy, A., Ohtani, E. & Yaxley, G. M. Solidus of alkaline carbonatite in the deep mantle. Geology **41**, 79-82 (2013).
30. Kuritani, T. et al. Buoyant hydrous mantle plume from the mantle transition zone. Sci. Rep. **9**, 6549 (2019).
31. Green II, H. W., Chen, W.-P. & Brudzinski, M. R. Seismic evidence of negligible water carried below 400-km depth in subducting lithosphere. Nature **467**, 828-831 (2010).
32. Mazza, S. E. et al. Sampling the volatile-rich transition zone beneath Bermuda. Nature **569**, 398-403 (2019).
33. Wang, X.-J. et al. Mantle transition zone-derived EM1 component beneath NE China: Geochemical evidence from Cenozoic potassic basalts. Earth Planet. Sci. Lett. **465**, 16-28 (2017).
34. Kuritani, T., Ohtani, E. & Kimura, J. I. Intensive hydration of the mantle transition zone beneath China caused by ancient slab stagnation. Nat. Geosci. **4**, 713-716 (2011).
35. Rohrbach, A. & Schmidt, M. W. Redox freezing and melting in the Earth's deep mantle resulting from carbon-iron redox coupling. Nature **472**, 209 (2011).
36. Soltanmohammadi, A. et al. Transport of Volatile-rich Melt from the Mantle Transition Zone via Compaction Pockets: Implications for Mantle Metasomatism and the Origin of Alkaline Lavas in the Turkish–Iranian Plateau. J. Petrol. **59**, 2273-2310 (2018).

Acknowledgements Taras Gerya provided the I2VIS code, and fruitful discussion with Andrea Marzoli, Christine Meyzen, Paolo Nimis, Davide Novella, Michele Lustrino, Konstantin Litasov, Shun-ichiro Karato and Xiaobing Xu are acknowledged. J.Y. was financially supported by Dipartimento di Geoscienze, Università di Padova. M.F. acknowledges the ERC StG #758199.

Author Contributions M.F. conceived the study. J.Y. performed all the numerical experiments and wrote the first draft of the paper. Both authors equally contributed to the discussion of the results and to the conclusions of this study.

Competing Interests The authors declare no competing interests.

Additional information

Extended data

Supplementary information

Reprints and permissions information is available at www.nature.com/reprints

Correspondence and requests for materials should be addressed to M.F.

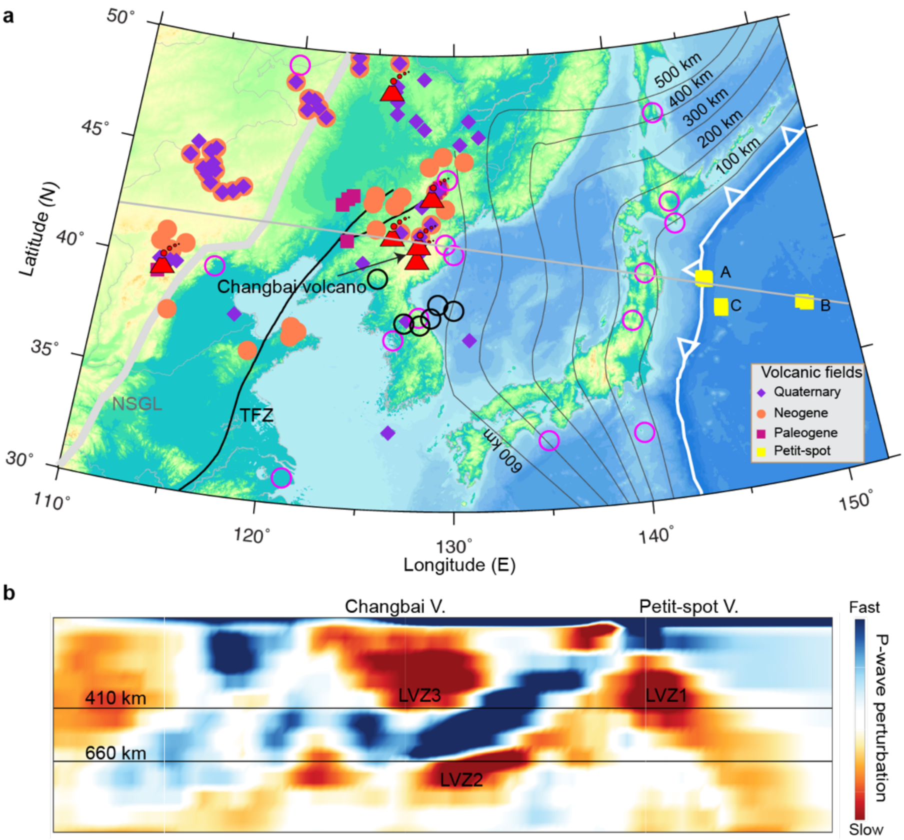

Figure 1 | Geological/Geophysical maps and Cenozoic volcanic fields in northeast China and offshore Japan. a, the red triangles denote volcanoes, the black and magenta circles show seismic low velocity at the 410 km and below 660 km, respectively, as determined by receiver functions[9,11,12]. Three young alkaline basalt sites (A, B, C) offshore the Japan trench known as petit-spot. The black contour lines indicate the Pacific Plate depths in the mantle. The present-day Pacific Plate front lies between the Tanlu Fault Zone (TFZ) and the North-South Gravity Lineament (NSGL). The map is created with open software GMT 5.4.3 which is under a GNU Lesser General Public License. **b**, cross-section (grey line in **a**) of seismic P-wave velocity perturbation with three distinct low velocity zones[8].

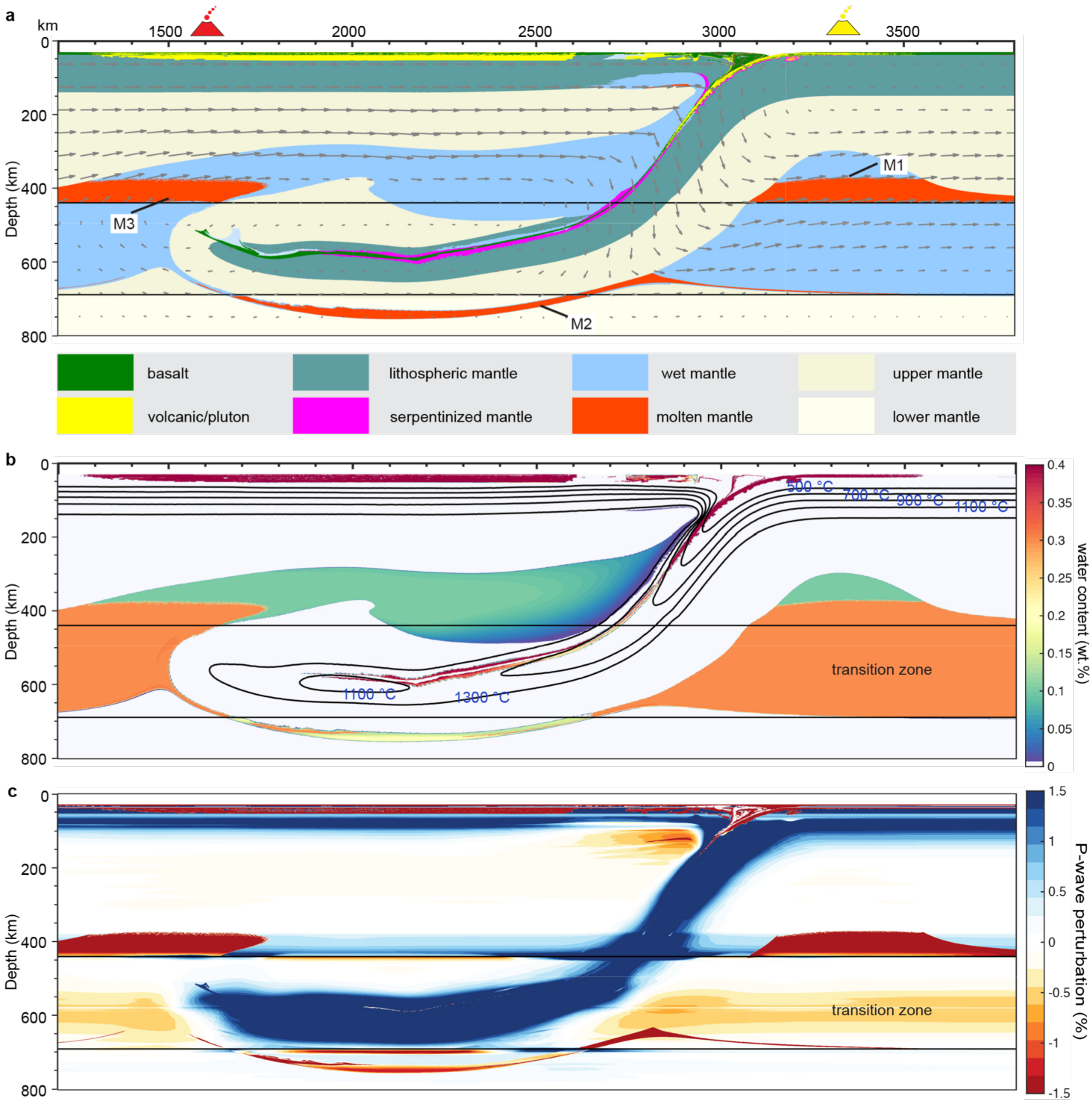

Figure 2 | Dynamics of subdution-induced dehydration melting above and below the transition zone. **a**, composition field and colors indicating different rock types at the bottom. Two black lines mark depths of 410-km and 660-km. Three partially molten regions (M) are indicated. **b**, water content with temperature contours and **c**, seismic P wave velocity anomalies. An initial water content of 0.3 wt.% is assumed in the MTZ and t_{ref}=6 kyr.

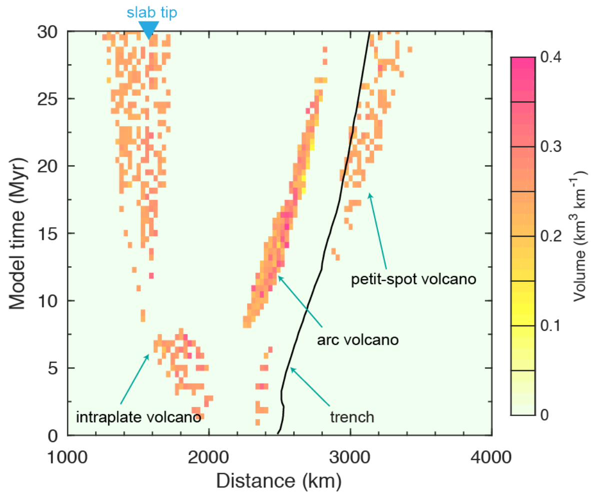

Figure 3 | Volcanics volume versus time. The volcanics include arc volcanoes by shallow decompression/hydrous melting and intraplate/petit-spot volcanoes by wet deep upper mantle melting. The trench location (black line) through the model evolution and the final location of the slab tip (inverted blue triangle) are also indicated.

Methods

Modelling approach. The 2-D petrological-thermo-mechanical numerical code I2VIS used in this study is based on a finite difference method employing marker-in-cell technique on a staggered grid[37]. It solves mass, momentum and energy conservation equations (eq. 1-3) on the Eulerian grid, and interpolates physical properties to the markers for advection accordingly.

$$\frac{\partial v_i}{\partial x_i} = 0 \quad (1)$$

$$-\frac{\partial P}{\partial x_i} + \frac{\partial}{\partial x_j}\left(\eta\left(\frac{\partial v_i}{\partial x_j} + \frac{\partial v_j}{\partial x_i}\right)\right) + \rho g_i = 0 \quad (2)$$

$$\rho c_p\left(\frac{\partial T}{\partial t} + v_i\frac{\partial T}{\partial x_i}\right) = \frac{\partial}{\partial x_i}\left(k\frac{\partial T}{\partial x_i}\right) + H_r + H_s + H_a \quad (3)$$

where v_i is velocity, x_i coordinate, P dynamic pressure, ρ density, g gravity acceleration, c_p heat capacity, T temperature, k thermal conductivity, H_r radioactive heating, $H_s = \tau_{ij}\dot{\varepsilon}_{ij}$ shear heating and adiabatic heating $H_a = T\alpha\frac{DP}{Dt}$. The latent heat is implicitly considered by computing the effective thermal expansion and heat capacity.

Model configuration. The initial model setup (6000 × 1000 km discretized with 1501 × 501 nodes) is composed of a 3500 km subducting plate and a 2500 km overriding plate. The model imposes free-slip mechanical boundary condition at the top with 30-km-thick and viscosity of 10^{18} Pa s 'sticky-air' to mimic free surface; the bottom boundary is no slip, and side boundaries are periodic. The bottom no-slip condition is needed to define an initial horizontal velocity from which finite differences can be computed for this variable. Comparison with results from a model with bottom free-slip condition and closed vertical walls indicate that the bottom no-slip boundary condition does not affect at all the subduction dynamics as it is confined above the lower mantle. The initial thermal structure is defined by the half-space cooling age for the plates (50 Myr old) and an adiabatic thermal gradient of 0.5 K/km for the underlying mantle. The thermal boundary conditions are isothermal on the top and bottom, while side boundaries are periodic consistently with the mechanical boundary conditions. To initiate subduction, the subducting slab extends down to ~200 km in the upper mantle together with a rheologically weak zone on top of it which lubricate the initial plates contact. The employed high numerical resolution (4 km × 2 km) is needed to ensure plate contact lubrication at shallow depths and localized, bending-related hydration at the trench outer-rise. Tests with a lower resolution (4 km × 4 km) results in a less localized slab mantle hydration, while with an 8 km × 4 km resolution self-sustained subduction and slab rollback do not appear spontaneously.

Viscous-plastic rheological model. The rock mechanical behaviour is represented by the effective viscosity which combines ductile (dislocation, diffusion and Peierls creep) and brittle (Drucker-Prager) deformation. The effective ductile viscosity is given by the harmonic average of the combined rheologies (parameters and physical meaning are defined in Extended Data Table 1):

$$\eta_{ductile} = (\frac{1}{\eta_{disl}} + \frac{1}{\eta_{diff}} + \frac{1}{\eta_{Peierls}})^{-1} \quad (4)$$

where the dislocation and diffusion creep are given by[38]:

$$\dot{\varepsilon} = A(\sigma/\mu)^n (b/d)^m \exp\,(-\frac{E+PV}{RT})\,\exp(\alpha\phi) \quad (5)$$

$$\eta = \frac{\sigma}{2\dot{\varepsilon}} \quad (6)$$

For hydrated (wet) mantle, viscosity is reduced by $\eta_{wet} = \eta_{dry}\left(\frac{C_W}{C_{W0}}\right)^{-r/n}$, and C_W, C_{W0} are water content and reference water content (100 ppm, which is the water content for the dry upper mantle), respectively.

The Peierls creep is given by[39]:

$$\eta_{Peierls} = 0.5 A_p \sigma_{II}'^{-1} \exp\,(\frac{E_{Peierls}+PV_{Peierls}}{RT}(1-(\frac{\sigma_{II}'}{\sigma_{Peierls}})^p)^q) \quad (7)$$

Brittle behaviour occurs when stresses are above the plastic yield stress τ_y:

$$\eta_{ductile} \leq \frac{\tau_y}{2\dot{\varepsilon}_{II}} \quad (8)$$

$$\tau_y = C + \mu P \quad (9)$$

Petrological modelling. Petrological solid-solid phase changes are included through the density and enthalpy look-up tables for basalt and pyrolite obtained from PERPLE_X[40]. Therefore, major phase transition boundaries at 410 km and 660 km have been considered.

The solidus ($T_s = f(P, T, H_2O)$) and liquidus ($T_l = f(P, T)$) temperatures for the upper mantle and MTZ are taken from high-pressure experiments[41] (Extended Data Fig. 1). At lower mantle conditions T_s and T_l vary considerably among different experiments. Here we adopt the dry solidus and liquidus of chondritic mantle[43] which are relatively more compatible with the results of KLB-1 peridotite[44], while the wet solidus[45] was measured on samples with an estimated water content of 400 ppm wt.

A conservative estimate of the melt fraction in the wet upper mantle[18] is applied:

$$\phi = \frac{W_a - W_{ol}}{W_m - W_{ol}} \tag{10}$$

where W_a, W_{ol} and W_m (10 wt. %) are water mass fraction of the ambient mantle, olivine and melt, respectively. Note that the water solubility in olivine increases with pressure, therefore the melt fraction will decrease with depth if W_a remains constant (Extended Data Fig. 3).

The silicate melt density (Extended Data Fig. 2) is from high-pressure sink-float experiments[53], which show that melt density becomes denser than the surrounding mantle at around 400 km[53,54] due to the increased compressibility. However, the presence of water generally reduces melt density that is buoyant relative to solid mantle (see Extended Data Fig. 2), rendering melt extraction at this depth possible. Moreover, we also test the melt density from molecular dynamics simulations at high pressure conditions[56] (Extended Data Fig. 4f, 5d).

Melt extraction timescale. The distance over which the compaction rate decreases by a factor of *e* is the characteristic length scale of the compaction process and is known as compaction length δ_c:

$$\delta_c = \sqrt{\frac{K(\zeta + \frac{4}{3}\eta)}{\eta_f}} \tag{11}$$

where ζ and η are the effective bulk and shear viscosities, respectively, of the partially molten rock; η_f the fluid viscosity; K the permeability given by the empirical equation:

$$K = K_0 (\frac{\phi}{\phi_0})^n \tag{12}$$

where ϕ is the porosity (melt fraction); K_0 ($10^{-12}\ m^2$) the permeability at the reference porosity ϕ_0 (0.01), and n =3.

The relative migration velocity between the melt and the solid matrix is w:

$$w = \frac{K \Delta\rho g}{\eta_f \phi} \tag{13}$$

thus, the extraction timescale t:

$$t = \frac{\delta_c}{w} = \frac{\phi}{\Delta\rho g}\sqrt{\frac{\eta_f(\zeta+\frac{4}{3}\eta)}{K}} \quad (14)$$

where $\zeta \approx \frac{\eta}{\phi}$, so $\zeta + \frac{4}{3}\eta \approx \frac{\eta}{\phi}$; if $\eta_f = 1\ Pa \cdot s$, then

$$t \approx \frac{1000}{\Delta\rho g\phi}\sqrt{\eta} \quad (15)$$

where $\Delta\rho$ is the density difference between the solid and melt, ranging from ~-100 to 270 kg/m^3 and typically ~70-180 kg/m^3 in the lowermost upper mantle if most of water is partitioned into melt, and the surrounding mantle viscosity $\eta = 10^{19} - 10^{20} Pa \cdot s$ in the upper mantle. For melt fraction $\phi = 0.02$, the estimated timescale would be t_{ref}≈3-20 kyr. Note that this timescale is not the time for melt migration to the surface, but only illustrates the efficiency of melt segregation from the solid matrix and the likelihood of its emplacement at shallow depths. Indeed, a small migration time implies a large $\Delta\rho$ (i.e., high buoyancy force) and/or high melt fraction (i.e., high permeability) and/or weak solid matrix which can be easily deformed during compaction/decompaction processes. In this study, we use a reference value t_{ref}=6 kyr. Melt extraction does not only depend on these three parameters (and fluid viscosity), but also on the dihedral angle (i.e., melt interconnectivity). Previous experiments showed that the dihedral angle decreases systematically with increasing pressure such that it probably allows for complete wetting at ~400 km[61] where the dihedral angle is <5°[62]. At these depths, melt interconnectivity is high even for low amounts of melt (<1%), which makes melt extraction possible provided the extraction timescale is sufficiently low. As such, when the extraction timescale t is smaller than t_{ref}, the material is extracted at the surface forming plutonic intrusions or volcanics[63]. Note that when the melt density is larger than solid surrounding mantle between 11.5 and 13.5 GPa when water content is low[53] (Extended Data Fig. 2b), there will be no melt extraction. In these conditions, the denser melt should percolate downward and accumulate over the 410-km discontinuity[18]. However, dry melting is generally not occurring at ambient mantle conditions except for an abnormal heat source associated with a mantle plume. As hydrogen partition preferentially into the melt, the water content in the melt would be quite high decreasing its density[53,54,62]. As a result, hydrous melt should be less dense than the solid matrix throughout the upper mantle[53].

The melt migration process is here illustrated with more realistic models accounting for visco-elasto-plastic deformation in a two-phase flow regime. These models demonstrate that melt migration from the deep upper mantle to the surface should occur through several mechanisms: viscous diapirism, viscoplastic decompaction channels and elasto-plastic dyking[64,65] (Extended Data Fig. 6). For a weak host rocks where viscous deformation dominates, such as asthenosphere, magma migrates by diapirism. When the magma moves through the lithosphere-asthenosphere boundary (or the lower crust in continents) where both ductile and brittle deformation occur, the fluid compaction pressure might reach the tensile strength and magma migrates by channeling. If the host rock is completely elasto-plastic, such as the core of lithospheric mantle and upper crust, magma migrates by dyking.

Water budget. The phase diagram reporting the maximum water content that can be hosted in hydrated or wet (i.e., absorbed by Nominally Anhydrous Minerals, NAMs) mantle rocks is built upon the compilation from refs 41, 55 (Extended Data Fig. 3). It is often assumed that heterogeneously serpentinized mantle rocks below the oceanic Moho can contain up to 2 wt. % H_2O[66,67]. As such, the maximum water content in hydrated rocks[55] is scaled accordingly.

As the oceanic crust completely dehydrates at about 300 km depth[41] generating fluids that fuel arc-volcanism only, we assume a dry crust for the sake of simplicity. On the other hand, dehydration of the underlying mantle within the transition zone is thought to cause intracontinental magmatism[15]. Consequently, we allow for serpentinization by bending-related deformation when the strain of mantle rocks is greater than 0.1[67].

When the rock water content exceeds the saturation limit, decomposition of hydrous minerals or water exsolution in NAMs occurs and fluid markers are generated and migrate according to the Darcy's law[67,68] until they are absorbed by dry markers:

$$V_i^f = V_i^s - \frac{\nabla P - \rho_f g_i}{(\rho_s - \rho_f) g_y} V_0 \tag{16}$$

where V_i^s, V_i^f, are velocities of solid and fluid phases, respectively; ρ_s, ρ_f are densities of solid and fluid, respectively; V_0 is a constant percolation velocity.

Upon partial melting and extraction, the water is partitioned into the extracted melt and water in the residual peridotite as:

$$C_w^{melt} = \frac{C_w}{\phi(1-D)+D} \tag{17}$$

$$C_w^{res} = \frac{C_w - \phi C_w^{melt}}{(1-\phi)} \tag{18}$$

where $D = 0.01$ is the hydrogen partition coefficient for olivine polymorphs.

Falling block tests. The validity of the employed petrological model can be easily tested with a simple model that a falling block (simulating the subducting slab) sinks into the wet MTZ exciting wet upwellings to the upper mantle and squeezing water into the lower mantle (Extended Data Fig. 4). These tests indicate that the melt layer gets thicker (>100 km) when melt extraction is not efficient owing to very small amounts of melt/water and/or denser melt phase. This might explain thick low velocity layers above the 410 km in many regions[9]. After melt extraction, less water remains above the transition zone causing higher viscosity and less melt fraction, which yields larger extraction timescale, i.e., the melt is preferentially ponding above the 410-km depth.

Seismic velocity anomalies. The seismic velocity perturbation in Fig. 2c have been computed as:

$$\delta \ln V = \frac{V - V_{ref}}{V_{ref}} \tag{19}$$

where V_{ref} is the average seismic velocity at specific depth.

The change of seismic wave velocities caused by the existence of a fluid phase is given by:

$$\frac{V_s}{V_s^0} = \frac{\sqrt{N/\mu}}{\sqrt{\bar{\rho}/\rho}} \tag{20}$$

$$\frac{V_p}{V_p^0} = \frac{\sqrt{\frac{K_{eff}}{k} + (4\gamma/3)N/\mu}}{\sqrt{1+4\gamma/3}\sqrt{\bar{\rho}/\rho}} \tag{21}$$

where

$$\frac{K_{eff}}{k} = \frac{K_b}{k} + \frac{(1-K_b/k)^2}{1-\phi-K_b/k+\phi k/k_f} \tag{22}$$

and $\gamma = \frac{\mu}{k} = \frac{3(1-2\upsilon)}{2(1+\upsilon)}$, V_s^0, V_p^0 are the shear and compressional wave velocities of the solid phase; k, μ, υ and ρ are bulk modulus, shear modulus, Poisson's ratio and density of solid phase, respectively. $\bar{\rho} = (1-\phi)\rho + \phi\rho_f$ is the effective density when fluid (e.g., melt) exists and the fluid density ρ_f. K_b and N are bulk and shear moduli which are dependent on melt fraction, dihedral angle[69]:

$$K_b = (1-\phi)k(1-(1-\varphi)^{n_k}) \tag{23}$$

$$N = (1-\phi)\mu(1-(1-\varphi)^{n_\mu}) \tag{24}$$

where

$$n_k = a_1\varphi + a_2(1-\varphi) + a_3\varphi(1-\varphi)^{1.5} \tag{25}$$

$$n_\mu = b_1\varphi + b_2(1-\varphi) + b_3\varphi(1-\varphi)^2 \tag{26}$$

and φ is the dihedral angle

$$\varphi = \frac{2A_{ss}}{2A_{ss}+A_{sl}} \tag{27}$$

and A_{ss}, A_{sl} are the area of solid-solid contact and solid-liquid contact, respectively[70].

Extended Data Fig. 7 shows $\mathrm{K_b}/\mathrm{k}$ and N/μ for the equilibrium geometry model at various dihedral angles.

Methods references

37. Gerya, T. V. & Yuen, D. A. Characteristics-based marker-in-cell method with conservative finite-differences schemes for modeling geological flows with strongly variable transport properties. Phys. Earth Planet. Inter. **140**, 293-318 (2003).

38. Karato, S.-i. & Wu, P. Rheology of the upper mantle: A synthesis. Science **260**, 771-778 (1993).

39. Kameyama, M., Yuen, D. A. & Karato, S.-I. Thermal-mechanical effects of low-temperature plasticity (the Peierls mechanism) on the deformation of a viscoelastic shear zone. Earth Planet. Sci. Lett. **168**, 159-172 (1999).

40. Connolly, J. Computation of phase equilibria by linear programming: a tool for geodynamic modeling and its application to subduction zone decarbonation. Earth Planet. Sci. Lett. **236**, 524-541 (2005).

41. Litasov, K. Physicochemical conditions for melting in the Earth's mantle containing a C–O–H fluid (from experimental data). Russ. Geol. Geophys. **52**, 475-492 (2011).

42. Litasov, K. D. & Ohtani, E. Phase relations in hydrous MORB at 18–28GPa: implications for heterogeneity of the lower mantle. Phys. Earth Planet. Inter. **150**, 239-263 (2005).

43. Andrault, D. et al. Melting of subducted basalt at the core-mantle boundary. Science **344**, 892-895 (2014).

44. Zhang, J. & Herzberg, C. Melting experiments on anhydrous peridotite KLB-1 from 5.0 to 22.5 GPa. J. Geophys. Res.: Solid Earth **99**, 17729-17742 (1994).

45. Nomura, R. et al. Low core-mantle boundary temperature inferred from the solidus of pyrolite. Science, **343**, 522-525 (2014).

46. Pradhan, G. K. et al. Melting of MORB at core–mantle boundary. Earth Planet. Sci. Lett. **431**, 247-255 (2015).

47. Andrault, D. et al. Solidus and liquidus profiles of chondritic mantle: Implication for melting of the Earth across its history. Earth Planet. Sci. Lett. **304**, 251-259 (2011).

48. Andrault, D. et al. Deep and persistent melt layer in the Archaean mantle. Nat. Geosci. **11**, 139 (2018).

49. Fiquet, G. et al. Melting of peridotite to 140 gigapascals. Science **329**, 1516-1518 (2010).

50. Boukaré, C. E., Ricard, Y. & Fiquet, G. Thermodynamics of the MgO-FeO-SiO2 system up to 140 GPa: Application to the crystallization of Earth's magma ocean. J. Geophys. Res.: Solid Earth **120**, 6085-6101 (2015).

51. Baron, M. A. et al. Experimental constraints on melting temperatures in the MgO–SiO2 system at lower mantle pressures. Earth Planet. Sci. Lett. **472**, 186-196 (2017).

52. Walter, M. J. et al. The stability of hydrous silicates in Earth's lower mantle: Experimental constraints from the systems MgO–SiO2–H2O and MgO–Al2O3–SiO2–H2O. Chem. Geol. **418**, 16-29 (2015).

53. Sakamaki, T., Suzuki, A. & Ohtani, E. Stability of hydrous melt at the base of the Earth's upper mantle. Nature **439**, 192-194 (2006).

54. Jing, Z. & Karato, S.-i. Effect of H2O on the density of silicate melts at high pressures: Static experiments and the application of a modified hard-sphere model of equation of state. Geochim. Cosmochim. Acta **85**, 357-372 (2012).

55. Iwamori, H. Phase relations of peridotites under H2O-saturated conditions and ability of subducting plates for transportation of H2O. Earth Planet. Sci. Lett. **227**, 57-71 (2004).

56. Guillot, B. & Sator, N. A computer simulation study of natural silicate melts. Part II: High pressure properties. Geochim. Cosmochim. Acta **71**, 4538-4556 (2007).

57. Sanloup, C. et al. Structure and density of molten fayalite at high pressure. Geochim. Cosmochim. Acta **118**, 118-128 (2013).

58. Bajgain, S., Ghosh, D. B. & Karki, B. B. Structure and density of basaltic melts at mantle conditions from first-principles simulations. Nat. Commun. **6**, 8578 (2015).

59. Agee, C. B. Crystal-liquid density inversions in terrestrial and lunar magmas. Phys. Earth Planet. Inter. **107**, 63-74 (1998).

60. Petitgirard, S. et al. Fate of MgSiO3 melts at core–mantle boundary conditions. Proc. Natl. Acad. Sci. **112**, 14186-14190 (2015).

61. Yoshino, T., Nishihara, Y. & Karato, S.-i. Complete wetting of olivine grain boundaries by a hydrous melt near the mantle transition zone. Earth Planet. Sci. Lett. **256**, 466-472 (2007).

62. Freitas, D. et al. Experimental evidence supporting a global melt layer at the base of the Earth's upper mantle. Nat. Commun. **8**, 2186 (2017).

63. Sizova, E., Gerya, T., Brown, M. & Perchuk, L. Subduction styles in the Precambrian: Insight from numerical experiments. Lithos **116**, 209-229 (2010).

64. Keller, T., May, D. A. & Kaus, B. J. P. Numerical modelling of magma dynamics coupled to tectonic deformation of lithosphere and crust. Geophys. J. Int. **195**, 1406-1442 (2013).

65. Lehmann, R. Modelling of Magma Dynamics from the Mantle to the Surface, Universitätsbibliothek Mainz (2016).

66. van Keken, P. E., Hacker, B. R., Syracuse, E. M. & Abers, G. A. Subduction factory: 4. Depth-dependent flux of H2O from subducting slabs worldwide. J Geophys Res.: Solid Earth **116** (2011).

67. Faccenda, M., Gerya, T. V. & Burlini, L. Deep slab hydration induced by bending-related variations in tectonic pressure. Nat. Geosci. **2**, 790-793 (2009).

68. Faccenda, M., Gerya, T. V., Mancktelow, N. S. & Moresi, L. Fluid flow during slab unbending and dehydration: Implications for intermediate-depth seismicity, slab weakening and deep water recycling. Geochem. Geoph.y Geosy. **13** (2012).

69. Takei, Y. Effect of pore geometry on Vp/Vs: From equilibrium geometry to crack. J. Geophys. Res.: Solid Earth **107**,6-12 (2002).

70. Bargen, N. & Waff, H. S. Permeabilities, interfacial areas and curvatures of partially molten systems: results of numerical computations of equilibrium microstructures. J. Geophys. Res.: Solid Earth **91**, 9261-9276 (1986).

Extended Data Table 1 | Physical properties of rocks used in this study.

Property	Symbol	Unit	Value
Gravity	g	m/s^2	9.81
Water content	C_w	wt. %	-
Reference water content	C_{w0}	wt. %	0.01
Melt fraction	ϕ	-	-
Melt-weakening factor	α	-	28
Shear modulus	μ	GPa	80
Diffusion creep			
prefactor	A	s^{-1}	8.7×10^{15}
Activation energy	E	kJ mol^{-1}	300
Activation volume	V	cm^3 mol^{-1}	6
Burgers vector	b	nm	0.5
Grain-size exponent	m	-	2.5
Water exponent	r	-	0.8
Dislocation creep			
prefactor	A	s^{-1}	3.5×10^{22}
Activation energy	E	kJ mol^{-1}	540
Activation volume	V	cm^3 mol^{-1}	20
Stress exponent	n	-	3.5
Water exponent	r	-	1.2
Peierls creep			
prefactor	A_P	Pa^2 s	$10^{4.2}$
Activation energy	E_{Peis}	kJ mol^{-1}	532
Activation volume	V_{Peis}	cm^3 mol^{-1}	12
Peierls stress	σ_{Peis}	GPa	9.1
Exponent	p, q	-, -	1, 2
Yield stress τ_y			
Cohesion	C	MPa	10
Friction coefficient	μ	-	0.6

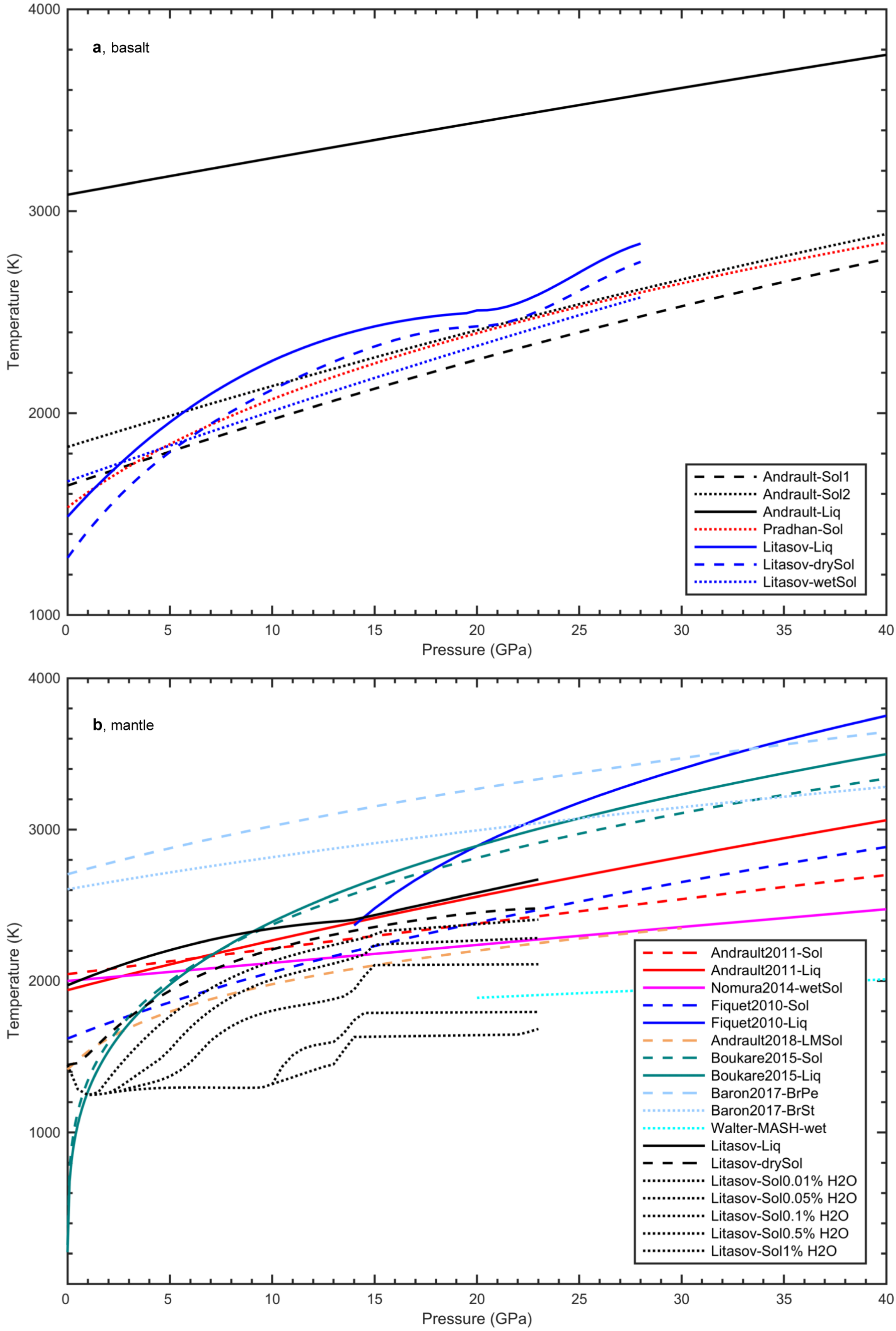

Extended Data Figure 1 | Solidus and liquidus of basalt and mantle. (**a**) The solidus and liquidus of basalt are obtained from experimental data[42,43,46]. The solidus from ref. 46 fits well within the uncertainty region by ref. 43 which is thus adopted. (**b**) Solidus and/or liquidus of mantle collected from literatures. The legends: *Sol*-solidus*,* *Liq*-liquidus, *BrPe*-

MgSiO$_3$-MgO (Bridgmanite + Periclase), *BrSt*-MgSiO$_3$-SiO$_2$ (Bridgmanite + Stishovite). Experimental data are from refs 41, 45, 47-52.

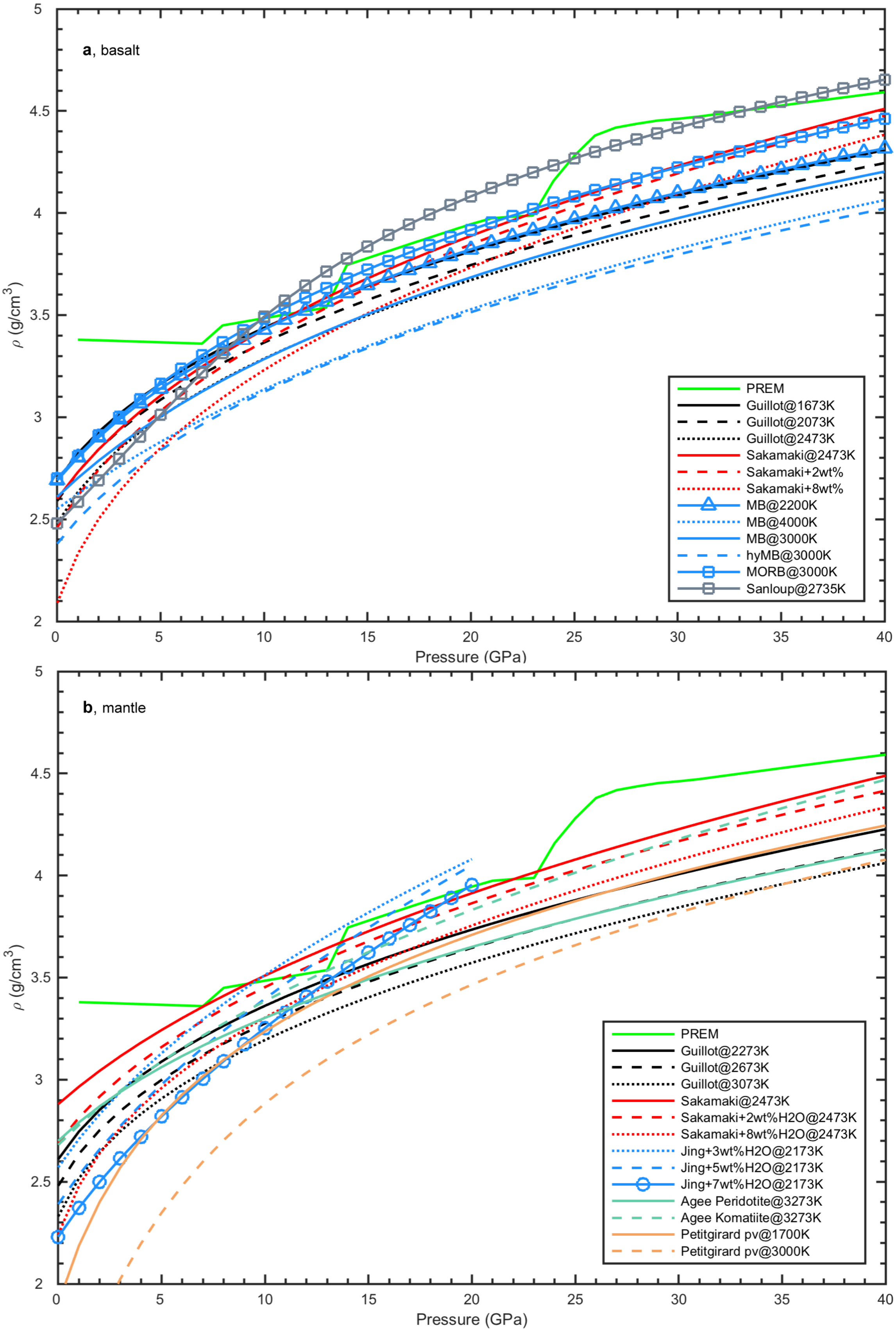

Extended Data Figure 2 | Melt density. Melt density of basalt (**a**) and mantle (**b**) for different temperatures and/or water contents. (**a**) *PREM*: density profile from Preliminary Reference Earth Model; dry melt density at temperatures of 1673 K, 2073 K and 2473 K[56], 2735 K[57]; dry and wet with 2 wt.% and 8 wt.% H_2O melt density at 2473 K[53]; the modeled basalt (MB), hydrated basalt (hyMB) and basalt (MORB)[58]. (**b**) Melt density of dry peridotite[56]; dry and wet (2 wt.% and 8 wt.% H_2O)[53]; wet peridotite (3 wt.%, 5 wt.%, 7 wt.% H_2O) [54]; dry peridotite and Komatiite[59] and perovskite[60]. Note the density crossover at around 13 GPa[53,54]. All the profiles are fitted by third- or forth-order of Birch-Murnaghan EoS.

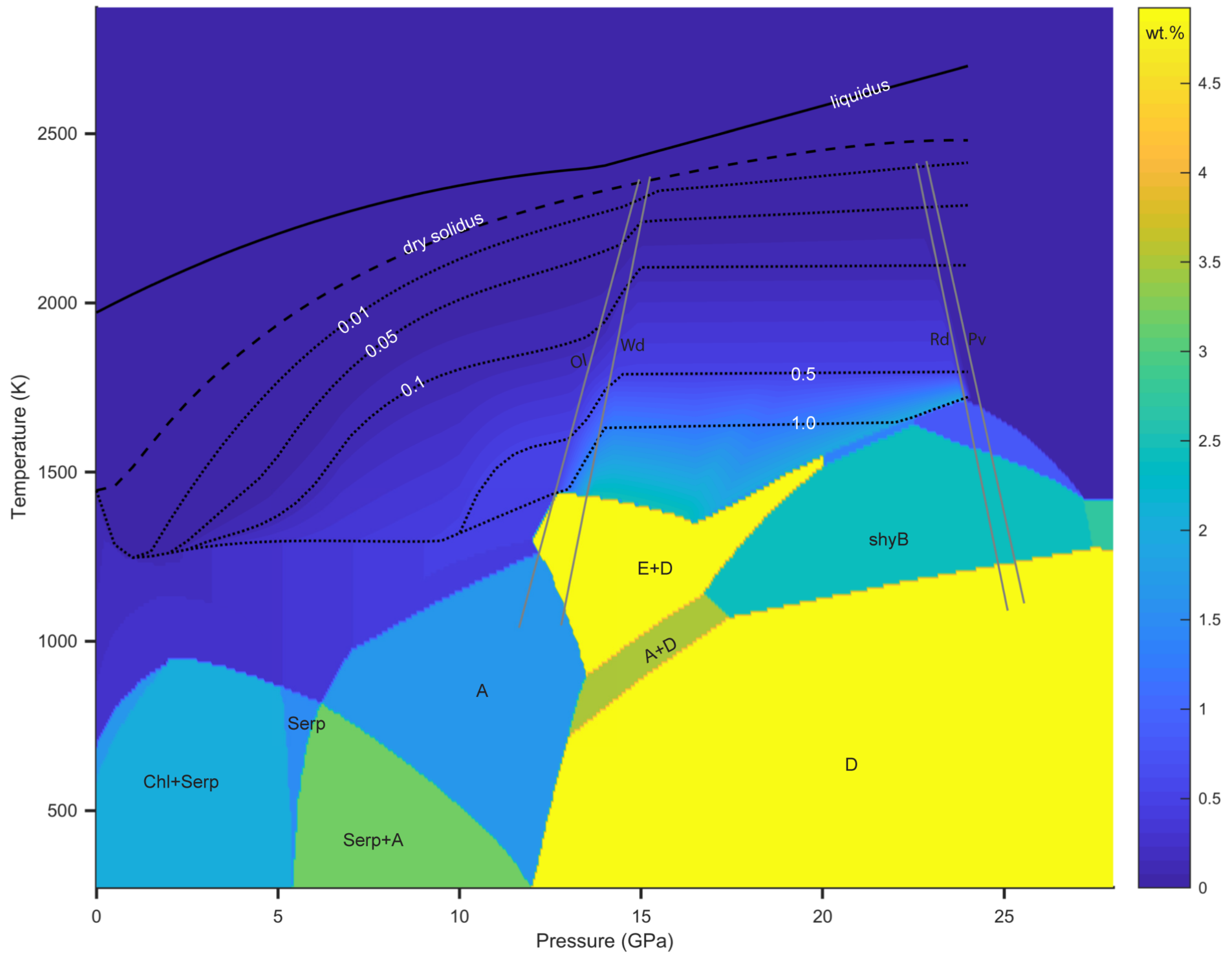

Extended Data Figure 3 | Phase diagram of H_2O-peridotite after ref. 55. The solidus/liquidus curves are the same in Extended Data Fig. 1. The grey lines are olivine-wadsleyite (Ol-Wd) and ringwoodite-perovskite (Rd-Pv) phase boundaries. The abbreviations of major hydrous phases are as follows: Chl-chlorite, Serp-serpentine, A-phase A, E-phase E, shyB-superhydrous phase B, D-phase D.

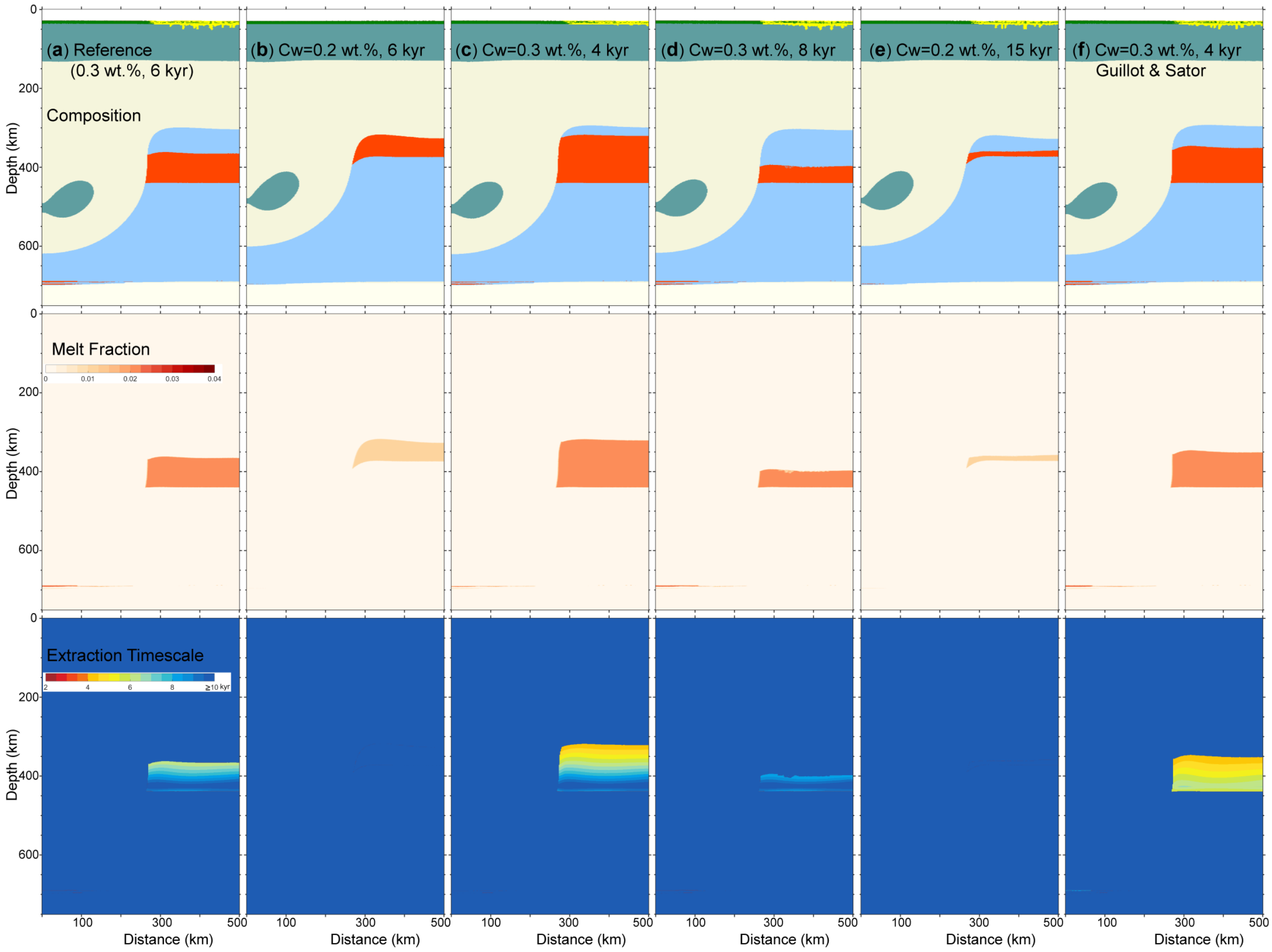

Extended Data Figure 4 | Falling block simulations with different parameters. (**a**) Reference model with initial MTZ water content of 0.3 wt.%, melt density from ref. 53 and reference extraction timescale t_{ref}=6 kyr. Other tests are similar to this model except for (**b**) initial water content Cw=0.2 wt.%, (**c**) extraction timescale t_{ref}=4 kyr, (**d**) t_{ref}=8 kyr, (**e**) Cw=0.2 wt.% and t_{ref}=15 kyr, (**f**) Cw=0.3 wt.% and t_{ref}=4 kyr by using the melt density from ref. 56. Note that the extraction timescale is calculated only when the melt is less dense than the solid matrix.

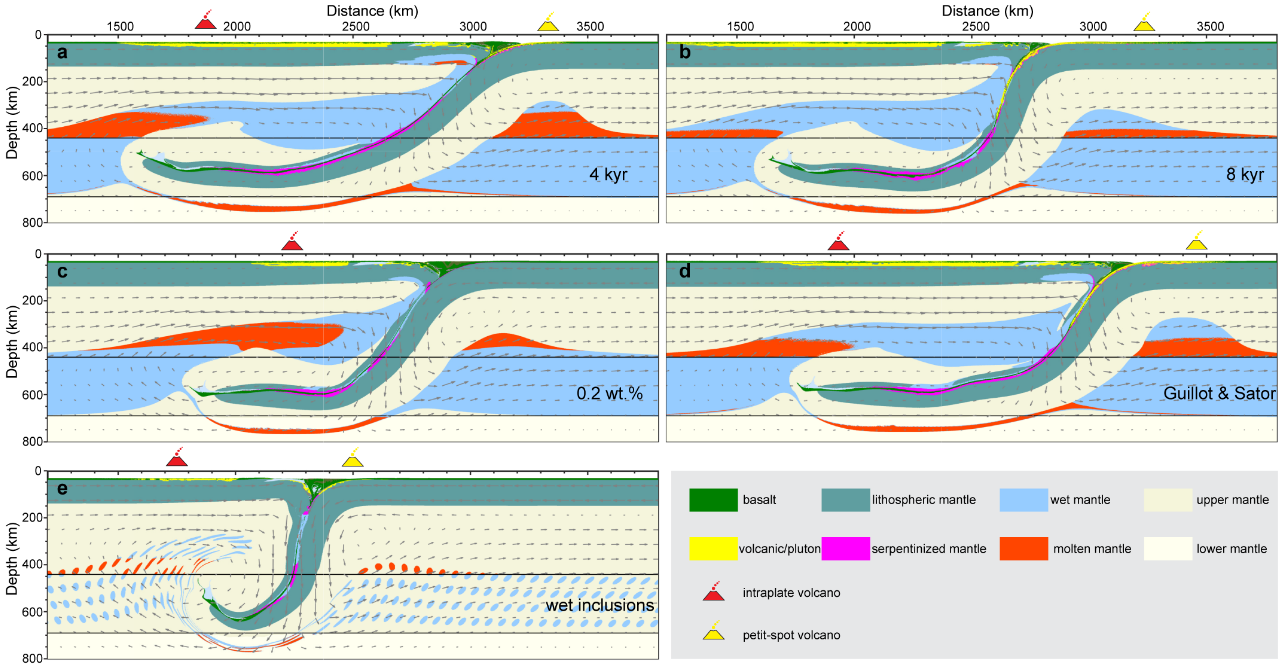

Extended Data Figure 5 | Additional parameter tests. Extraction timescale of 4 kyr in (**a**) and 8 kyr in (**b**) with 0.3 wt.% initial water content. A 0.2 wt.% initial water content in (**c**). Melt density from ref. 56 and t_{ref}=4 kyr in (**d**). (**e**), wet inclusions in the transition zone with t_{ref}=6 kyr. Note that all the models differ by only one particular parameter compared to the reference model (Fig. 2) except (**d**).

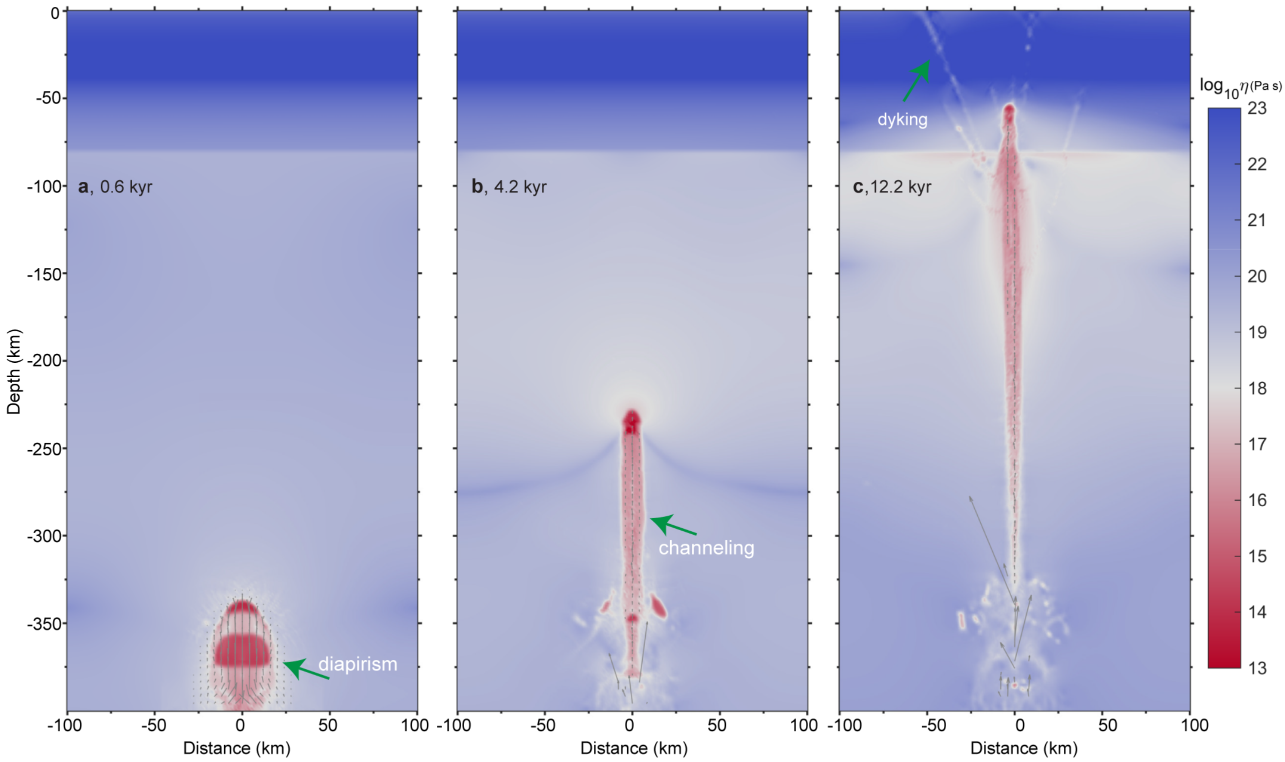

Extended Data Figure 6 | Visco-plastic shear viscosity for melt percolation in two-phase flow. Melt percolation at three typical stages as (**a**), diapirism (**b**), channeling and (**c**), dyking from deep mantle to the surface. The numerical 2D finite element code MVEP2 (https://bitbucket.org/bkaus/mvep2) was used to simulate melt migration dynamics. A small background strain rate (10^{-15} s^{-1}, the model domain has been extended by only 0.75 km after 12.2 kyr) was applied at the side boundaries and top boundary is free surface. An initial porosity at the bottom boundary with Gaussian distribution (results in an average porosity of 0.127) was applied. The details of the approach allowing for its reproduction are provided elsewhere[64,65].

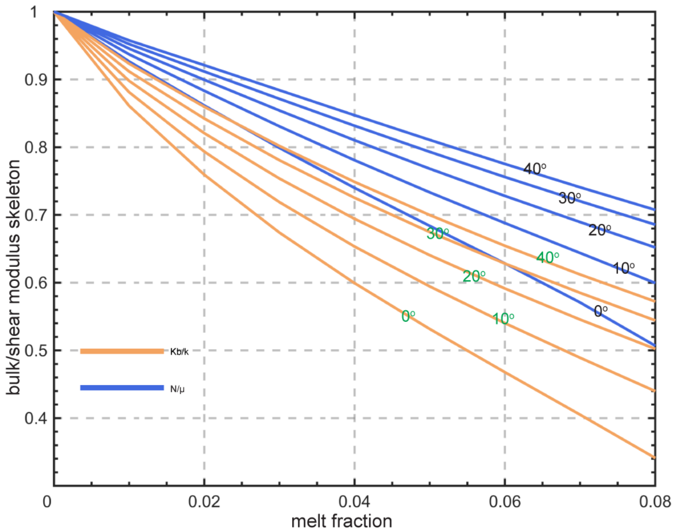

Extended Data Figure 7 | Normalized bulk modulus (K_b/k) and shear modulus (N/μ) of skeleton versus melt fraction. The ratios of wet and dry of bulk/shear modulus are decreasing with melt fraction. The numbers show on the lines are dihedral angles.

* manuele.faccenda@unipd.it